ELSEVIER

Prediction of turbulent transitional phenomena with a nonlinear eddy-viscosity model

T. J. Craft, B. E. Launder, and K. Suga
Department of Mechanical Engineering, UMIST, Manchester, England

This paper describes a new nonlinear eddy-viscosity model of turbulence designed with a view to predicting flow far from equilibrium, including transition. The scheme follows earlier UMIST practice in adopting a cubic relation between the stress and the strain/vorticity tensors but broadens the range of flows to which the model applies by including a third transport equation for an anisotropy parameter of the stress field. Applications are shown for transition on a flat plate at different levels of free-stream turbulence, for the normal impingement of a turbulent jet on a flat plate, and for the flow around a turbine blade. The model is shown to generate much more realistic predictions than what is said to be the best of the linear eddy-viscosity schemes.

Keywords: turbulence model; non-linear eddy viscosity; transition; turbine blade

Introduction

It is now well established that the process of transition from a laminar to a turbulent boundary layer in the presence of substantial free-stream turbulence is one that lends itself better to prediction by "turbulence modelling" than by stability analysis. The first demonstration of such transition prediction was by C. H. Priddin (see Launder and Spalding 1974), while later Scheuerer (1983) reported a more extensive study. Both these schemes adopted standard low-Reynolds-number k–ε models.

More recently, Savill (1993, 1995) has been coordinating a major (largely) European effort in establishing, conclusively, the strengths and weaknesses of solvers of different types in predicting the phenomenon commonly referred to nowadays as "by-pass" or "diffusion-controlled" transition. The series of reports springing from that collaborative exploration make essential background reading and cannot be summarized in a sentence or two. A very important development, however, has been the increasing tendency to start computations ahead of the solid body on which transition occurs—something that has become possible with the great increase of the core memory readily available—and the consequent use of *elliptic* (rather than parabolic) solvers. Not only does this mean that uncertainties in initial conditions have far less impact than with a parabolic solver—since inlet conditions are imposed *upstream* of the plate or blade on which transition actually occurs; it also means that the turbulence model has to cope with a more complex strain field than just a simple shear, since, in the vicinity of the stagnation point at the leading edge, the flow departs strongly from a simple shear. (Downstream from the leading-edge region, the flow may again be adequately described by the parabolic equations, although, if the transition itself is abrupt, retention of streamwise diffusion may be significant in the vicinity of the transition "point" itself.) Both these developments have helped underline the point that simple two-equation eddy-viscosity schemes—for all their attractiveness from the point of view of economy—do not offer a sufficiently capacious framework to predict the physical phenomena over a useful width of conditions.

Second-moment closures offer a far more general route, although, despite continuing decreases in computing cost, they are still seen as too complicated for routine industrial applications. Thus, it is to *nonlinear* eddy-viscosity schemes that several groups are now looking to bring realism in computational fluid dynamics (CFD) predictions to engineering flows. While such approaches have a history of more than 20 years (Pope 1975), there has been a particular concentration of activity over the last half-dozen or so. Nearly all schemes have taken the stress proportional to quadratic products of strain and vorticity. In our earlier papers on this topic (Craft et al. 1993, 1996), however, it is pointed out that cubic-level contributions are needed to give the predicted stress field approximately the correct sensitivity to minor strains.

In planning the extension of this earlier work to the problems of diffusion-controlled transition, one serious anomaly was that, for the case of fully developed pipe or channel flow, the model of Craft et al. (1996) predicted levels of the turbulence intensities with much too little difference among components (Figure 1). This failure was particularly serious for the component normal to the wall v, which is particularly important in determining turbulent heat fluxes (see Equation 2 below). The conclusion reached was that some parameter other than the turbulent Reynolds number was needed on which the turbulence model coefficients could be allowed to depend. Now, modern second-moment closures make some of their coefficients dependent on certain of

Address reprint requests to Dr. B. E. Launder, Department of Mechanical Engineering, UMIST, P.O. Box 88, Manchester, M60 1QD, UK.

Received 10 March 1996; accepted 15 October 1996

Int. J. Heat and Fluid Flow 18: 15–28, 1997

655 Avenue of the Americas, New York, NY 10010

0142-727X/97/$17.00
PII S0142-727X(96)00145-3

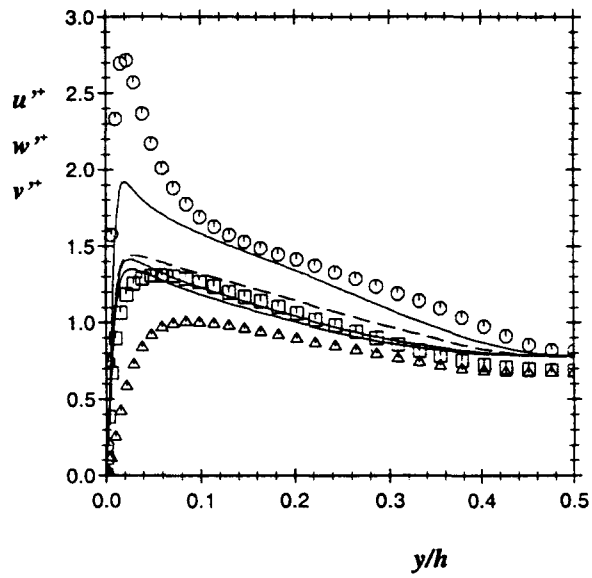

Figure 1 Turbulence intensity profiles in fully developed flow in a plane channel (normalized with wall parameters), Re=13,750; symbols: DNS results, Kim (1989), ○: u', □ $-w'$; Δ $-v'$ ——: predicted with two-equation N-LEVM, Craft et al. (1996); ----: predictions with linear EVM (all three intensities equal)

the stress invariants (e.g., Lumley 1978; Launder and Tselepidakis 1993; Craft and Launder 1995) and a similar approach has therefore been adopted with our N-LEVM also.

In the development below the following section provides a statement of the currently adopted model. Thereafter, consideration is first given to applications of the model not involving transition phenomena. (Since most transitional flows reach a fully turbulent state, it is essential that the model should also apply in that limit.) Thereafter, applications are considered in turn of transition on a flat plate; the turbulent impinging jet; and, finally, the flow around a turbine blade. The paper ends by considering potential for further development.

The proposed closure

To provide a full account of both the model and the rationale leading to particular forms would require more space than is available here. Such a complete presentation is provided by Suga's Ph.D. thesis (also available in report form, Suga 1996); it is hoped, therefore, that the limited account below adequately meets immediate needs. There are three areas where particular attention is needed: the basic constitutive equation for the Reynolds stress $\overline{u_i u_j}$ and the heat flux $\overline{u_i \theta}$; the substantially modified transport equation for ε; and the transport equation for the stress-invariant, A_2. These form the subjects of succeeding sections.

The constitutive equation for $\overline{u_i u_j}$

The following constitutive equation is adopted for the dimensionless anisotropic Reynolds stress tensor $a_{ij} \equiv (\overline{u_i u_j} - \frac{2}{3}\delta_{ij}k)/k$, k being the turbulent kinetic energy, $(1/2)\overline{u_k u_k}$.

$$a_{ij} = -\frac{\nu_t}{k}S_{ij} + c_1\frac{\nu_t}{\tilde{\varepsilon}}\left(S_{ik}S_{kj} - \frac{1}{3}S_{kl}S_{kl}\delta_{ij}\right) + c_2\frac{\nu_t}{\tilde{\varepsilon}}(\Omega_{ik}S_{kj} + \Omega_{jk}S_{kl}) + c_3\frac{\nu_t}{\tilde{\varepsilon}}\left(\Omega_{ik}\Omega_{jk} - \frac{1}{3}\Omega_{lk}\Omega_{lk}\delta_{ij}\right)$$

Notation

a_{ij}	normalized stress anisotropy $(\overline{u_i u_j} - \frac{2}{3}\delta_{ij}k)/k$
A^*	a surrogate form of A, see Equation 8 et seq.
A_3	$a_{ij}\ a_{jk}\ a_{kl}$
A	$1-(9/8)(A_2-A_3)$
c_f	skin friction coefficient
d_ϕ	diffusion rate of $\phi(\phi \equiv k, \tilde{\varepsilon}, \overline{u_i u_j})$
D	diameter of impingement pipe
H	boundary-layer shape factor (displacement thickness/momentum thickness)
k	turbulence kinetic energy
ℓ_f	a length scale, Equation 9
M_s	isotropic Mach number
Nu	Nusselt number
P	mean pressure
P_{ij}, P_k	shear production rate of $\overline{u_i u_j}, k$
q_w	wall heat flux (kW/m^2)
r	radius
$\tilde{R}_t$	turbulent Reynolds number $k^2/\nu\tilde{\varepsilon}$
Re	mean flow Reynolds number $U_b D'/\nu$
$\tilde{S}$	dimensionless strain parameter, $(k/\tilde{\varepsilon})\sqrt{(1/2)S_{ij}S_{ji}}$
S_{ij}	mean strain-rate tensor $(\partial U_i/\partial x_j + \partial U_j/\partial x_i)$
U_k	mean velocity in direction x_k
U_b	bulk velocity in pipe
u', v', w'	root-mean-square turbulent velocities
x_k	Cartesian space coordinate-tensor notation (x_2 normal to wall, x_1 primary flow direction)
y	Cartesian coordinate normal to wall

Greek

ε	energy dissipation rate
$\tilde{\varepsilon}$	"homogeneous" dissipation rate, $\varepsilon - 2\nu(\partial k^{1/2}/\partial x_j)^2$
ε_{ij}	viscous dissipation rate of $\overline{u_i u_j}$
ν	kinematic viscosity
ν_t	linear part of turbulent viscosity $c_\mu k^2/\varepsilon$
ϕ_{ij}	pressure–strain contribution
Θ	mean temperature
Ω_{ij}	mean vorticity tensor, $[(\partial U_i/\partial x_j) - (\partial U_j/\partial x_i)]$
$\tilde{\Omega}$	dimensionless vorticity parameter, $(k/\tilde{\varepsilon})\sqrt{(1/2)\Omega_{ij}\Omega_{ij}}$

Subscripts

ex	exit values
i	inlet values
w	wall values

$$+c_4\frac{\nu_t k}{\tilde{\varepsilon}^2}(S_{ki}\Omega_{lj}+S_{kj}\Omega_{li})S_{kl}$$

$$+c_5\frac{\nu_t k}{\tilde{\varepsilon}^2}\left(\Omega_{il}\Omega_{lm}S_{mj}+S_{il}\Omega_{lm}\Omega_{mj}-\frac{2}{3}S_{lm}\Omega_{mn}\Omega_{nl}\delta_{ij}\right)$$

$$+c_6\frac{\nu_t k}{\tilde{\varepsilon}^2}S_{ij}S_{kl}S_{kl}+c_7\frac{\nu_t k}{\tilde{\varepsilon}^2}S_{ij}\Omega_{kl}\Omega_{kl} \qquad (1)$$

where

$$S_{ij}\equiv\frac{\partial U_i}{\partial x_j}+\frac{\partial U_j}{\partial x_i},\quad \Omega_{ij}\equiv\frac{\partial U_i}{\partial x_j}-\frac{\partial U_j}{\partial x_i}$$

$$\tilde{S}\equiv\frac{k}{\tilde{\varepsilon}}\sqrt{S_{ij}S_{ij}/2},\quad \tilde{\Omega}\equiv\frac{k}{\tilde{\varepsilon}}\sqrt{\Omega_{ij}\Omega_{ij}/2},\quad \nu_t=c_\mu\frac{k^2}{\tilde{\varepsilon}}$$

and $\tilde{\varepsilon}$ is the so-called isotropic dissipation rate of turbulence energy.

The recommended forms for the various coefficients are given in Table 1. The quantities $\tilde{R}_t$, η, and A_2 are, respectively, the turbulent Reynolds number $k^2/\nu\tilde{\varepsilon}$, $r_\eta\max\{\tilde{S},\tilde{\Omega}\}$ and the second invariant of the stress tensor $a_{ij}a_{ij}$. Equation 1 is a subset of the generalized nonlinear form given by Pope (1975). In fact, the terms with coefficients c_6 and c_7 are all incorporated under the linear term in Pope's presentation, since, in each case, the strain tensor S_{ij} multiplies invariants of the strain or vorticity field. Here, we prefer to make evident the different contributions by separately designating the coefficients as indicated.

The empirical coefficients are tuned by reference to a number of fundamental shear flows. The value of the coefficients c_2 and (c_1+c_3) are the only ones to affect the anisotropic normal stresses in a simple shear. The values given in Table 1 were optimized by considering both direct numerical simulation (DNS) and experimental data of homogeneous shear over a range of $\tilde{S}$ (from 3 to 18) together with the requirement that, no matter how large S might be, negative normal stresses should not arise. Likewise, matching the shear stress behavior in simple shear has led to our taking $(-c_5+c_6+c_7)$ equal to zero.

Further decisions on the coefficients were taken by reference to curved flows. Swirling pipe flow is known to produce a markedly nonlinear variation of swirl velocity with radius even in fully developed flow (Cheah et al. 1993). Only the terms with coefficient c_4 and c_5 can produce such a nonlinear variation; indeed the two terms lead to the same velocity gradient elements. By contrast, the sensitivity of the stress field to the effects of curvature strains in two-dimensional flow (2-D) (over a convex surface, say) are dependent on c_5 and c_7, and, again, the form of the cubic terms is identical for the two terms. Thus, for the present, c_5 has been taken as zero leaving c_4 and c_7 to be tuned by reference to the above-noted flows. Finally, it is noted that c_3 is assigned a functional form in order that, in solid-body rotation (where S is zero, but Ω is not) the rotation rate should have no effect on the resultant stress field.

It is perhaps not helpful to attempt a detailed comparison with previous proposals for the above coefficients. Our earlier study (Craft et al. 1996) showed that previous proposals, based on *quadratic* strain and vorticity elements had generated such a diversity in magnitude and, in some cases, sign of the coefficients that the only conclusion we could draw was that no widely applicable constitutive equation could be formulated at that level. That is why, in our earlier and present contributions, a cubic formulation has been adopted.

Turbulent heat fluxes

Earlier work on nonlinear eddy-viscosity models (EVMs) has generally adopted the turbulent-Pandtl number approach to determine the heat flux normal to the wall. Here, however, because of the considerable improvement in our ability to mimic the fluctuating velocity normal to the wall, the more widely applicable model of Daly and Harlow (1970) is adopted

$$\overline{u_i\theta}=-c_\theta\frac{k}{\varepsilon}\overline{u_iu_j}\frac{\partial\Theta}{\partial x_j} \qquad (2a)$$

If a plane wall lies in the x–z-plane, the expression for the turbulent heat flux normal to the wall is thus:

$$\overline{v\theta}=-c_\theta\frac{k}{\varepsilon}\overline{v^2}\frac{\partial\Theta}{\partial y} \qquad (2b)$$

The form of the coefficient c_θ has been chosen by reference to the DNS results of Kasagi et al. (1992):

$$c_\theta=\frac{0.3+0.2\sqrt{\hat{\varepsilon}/\varepsilon}}{1+0.5A_2^{0.5}+0.07A_2^3}$$

where

$$\hat{\varepsilon}\equiv 2\nu\left(\frac{\partial k^{1/2}}{\partial x_j}\right)^2$$

Table 1 The empirical coefficients

c_1	c_2	c_3	c_4	c_5	c_6	c_7
$-0.05\frac{f_q}{f_\mu}$	$0.11\frac{f_q}{f_\mu}$	$0.21\frac{f_q\tilde{S}}{f_\mu(\tilde{S}+\tilde{\Omega})/2}$	$-0.8f_c$	0	$-0.5f_c$	$0.5f_c$

c_μ	f_μ
$\frac{0.667r_\eta[1-\exp[-0.415\exp(1.3\eta^{5/6})]]}{1+1.8\eta}$	$\frac{1.1\sqrt{\tilde{\varepsilon}/\varepsilon}\,[1-0.8\exp(-\tilde{R}_t/30)]}{1+0.6A_2+0.2A_2^{3.5}}$

r_η	f_q	f_c
$1+[1-\exp[-(2A_2)^3]]\left[1+4\sqrt{\exp\left(-\frac{\tilde{R}_t}{20}\right)}\right]$	$\frac{r_\eta}{(1+0.0086\eta^2)^{1/2}}$	$\frac{r_\eta^2}{1+0.45\eta^{2.5}}$

The A_2 transport equation

The constitutive equation for $\overline{u_i u_j}$ section has introduced in a variety of ways the second invariant of a_{ij} into the stress strain formula. This we have found (using experimental values of A_2) had enabled the strongly individual variations of the components of $\overline{u_i u_j}$ to be realistically captured. However, our initial expectation that A_2 could simply be obtained by processing the resultant stress field proved to be seriously misplaced: that led to a near-wall stress field (and A_2 distribution) strongly at odds with the data. Accordingly, it was decided that the best route would be to determine A_2 from a transport equation. An exact transport equation for A_2 may easily be obtained by multiplying the transport equation for a_{ij} by $2a_{ij}$. The result may be written:

$$\frac{DA_2}{Dt} = -2\frac{A_2}{k}(d_k + P_k - \varepsilon) + 2\frac{a_{ij}}{k}(d_{ij} + P_{ij} + \phi_{ij} - \varepsilon_{ij}) \qquad (3)$$

where d_{ij}, P_{ij}, ϕ_{ij}, and ε_{ij} are, respectively, the diffusive transport, shear production, pressure redistribution, and dissipation rates of $\overline{u_i u_j}$, and d_k, P_k, and ε are half the corresponding contractions in the turbulence energy budget (the trace of ϕ_{ij} being zero).

In the above equation, P_{ij} and P_k denote, respectively, the mean strain generation rates of $\overline{u_i u_j}$ and k:

$$P_{ij} \equiv -\left(\overline{u_i u_k}\frac{\partial U_j}{\partial x_k} + \overline{u_j u_k}\frac{\partial U_i}{\partial x_k}\right); \quad P_k \equiv -\overline{u_i u_j}\frac{\partial U_i}{\partial x_j}$$

These terms need no further approximation. For ϕ_{ij} and ε_{ij}, adapted versions of models used in second-moment closure work at UMIST have been chosen. For the former, the usual practice of separately accounting for turbulence, mean-strain, and wall-reflection effects is followed:

$$\phi_{ij} = \phi_{ij1} + \phi_{ij2} + \phi^w_{ij} \qquad (4)$$

where

$$\phi_{ij1} = -\tilde{c}_1\varepsilon\left[a_{ij} + c'_1\left(a_{ik}a_{kj} - \frac{1}{3}A_2\delta_{ij}\right)\right] - \sqrt{A^*}\,\varepsilon a_{ij} \qquad (5)$$

$$\phi_{ij2} = -0.6\left(P_{ij} - \frac{1}{3}\delta_{ij}P_{kk}\right) + 0.3a_{ij}P_{kk} \qquad (6)$$

$$\begin{aligned}\phi^w_{ij} = {} & -c_{2w}\frac{\partial U_l}{\partial x_m}\overline{u_l u_m}\left(\frac{\partial \ell_f}{\partial x_q}\frac{\partial \ell_f}{\partial x_q}\delta_{ij} - 3\frac{\partial \ell_f}{\partial x_i}\frac{\partial \ell_f}{\partial x_j}\right) \\ & - c'_{2w}\left(a_{lm}\frac{\partial U_k}{\partial x_m}\frac{\partial \ell_f}{\partial x_l}\frac{\partial l_f}{\partial x_k}\delta_{ij} - \frac{3}{2}a_{lm}\frac{\partial U_i}{\partial x_m}\frac{\partial \ell_f}{\partial x_l}\frac{\partial \ell_f}{\partial x_j}\right. \\ & \left. - \frac{3}{2}a_{lm}\frac{\partial U_j}{\partial x_m}\frac{\partial \ell_f}{\partial x_l}\frac{\partial \ell_f}{\partial x_i}\right)k \\ & + c''_{2w}k\frac{\partial U_l}{\partial x_m}\frac{\partial \ell_f}{\partial x_l}\frac{\partial \ell_f}{\partial x_m}\left(\frac{\partial \ell_f}{\partial x_i}\frac{\partial \ell_f}{\partial x_i} - \frac{1}{3}\frac{\partial \ell_f}{\partial x_q}\frac{\partial \ell_f}{\partial x_q}\delta_{ij}\right)\end{aligned} \qquad (7)$$

In Equation 5

$$\tilde{c}_1 = 3.1\left(1 - \exp\left[-(\tilde{R}_t/80)^2\right]\right)\min\left(\sqrt{A_2}, 0.5\right)\sqrt{A^*}$$

$$c'_1 = 1.2$$

The quantity A^* is a surrogate for Lumley's stress flatness factor A (Lumley 1978) defined as $1 - (9/8)(a_{ij}a_{ji} - A_3)$, where A_3 is the third invariant $a_{ij}a_{jk}a_{ki}$, and the a_{ij} are implicitly computed from transport equations. The parameter A takes the value zero at the wall where turbulence goes to the two-component limit.

Now, with the N-LEVM that is the subject of the present contribution, one does not get a reliable level of this flatness factor merely by processing the predicted stress field using the definition of A. Accordingly, as indicated above, a simulated form A^* is processed. We take

$$A^* = f_A A' + (1 - f_A)A'' \qquad (8)$$

where A' and A'' are alternative approximations of A bridged by way of the function f_A, which is itself a function of A'':

$$f_A \equiv \exp(-20A''^2)$$

$$A' \equiv A\{1 - \exp[-\tilde{R}_t^2/(1 + 24A_2)]\}$$

$$A'' \equiv \left\{1 - \frac{9}{8}\left[A_2 - A_3(A_2/a_{ij}a_{ij})^{3/2}\right]\right\} \times \left\{1 - \exp\left[-(\tilde{R}_t/10)^1\right]\right\}\tilde{\varepsilon}/\varepsilon$$

where A is obtained from the computed anisotropic stress field using the definition above. Within the near wall region, A^* is essentially A', but in the outer part of a boundary layer, particularly in a complex strain field, A'' provides a better approximation. For the future, it is to be hoped that, as more experience is gained, a simpler form can be introduced.

Readers may note that Equation 6 is simpler than the usual form of ϕ_{ij2} adopted by the UMIST group. This is simply because, on multiplying Equation 6 by a_{ij} (viz. Equation 3), several terms vanished, while others were found to have negligible effect (Suga 1996). The form of ϕ^w_{ij} is an adaptation of that employed by Craft and Launder (1992). However, that form contained both unit vectors normal to the wall and wall distance —factors that can have physical significance only for a plane surface. Thus, in the present proposal, both these parameters were replaced by length-scale gradients. The length ℓ_f is given by:

$$\ell_f = \frac{1 - \exp-(\tilde{R}_t/30)}{1 + 3.5A_2^2}\frac{k^{3/2}}{\varepsilon} \qquad (9)$$

The simpler and more usual form: $k^{3/2}/\varepsilon$ is not useful, since this levels out (temporarily) in the buffer layer, thus making the contribution of ϕ^w_{ij} negligible in a region where it is greatly needed. The coefficients in Equation 7 take the following values:

$$c_{2w} = 0.088A_2^2; \quad c'_{2w} = 0.16A_2^2;$$

$$c''_{2w} = 1.2\left\{1 - \exp\left[-(\tilde{R}_t/80)^2\right]\right\}A_2^2$$

The general form of the dissipation tensor is also taken over from current second-moment modeling ideas. We take

$$\varepsilon_{ij} = f_\varepsilon\varepsilon^*_{ij} + (1 - f_\varepsilon)\frac{2}{3}\delta_{ij}\varepsilon \qquad (10)$$

where

$$\varepsilon_{ij}^{*}=\left[2\nu f_{\varepsilon}^{*}\frac{\partial k^{1/2}}{\partial x_m}\left(\frac{\overline{u_j u_m}}{k}\frac{\partial k^{1/2}}{\partial x_i}+\frac{\overline{u_i u_m}}{k}\frac{\partial k^{1/2}}{\partial x_j}\right)\right.$$

$$\left.+2\nu f_{\varepsilon}^{*}\frac{\partial k^{1/2}}{\partial x_k}\frac{\partial k^{1/2}}{\partial x_m}\frac{\overline{u_k u_m}}{k}\delta_{ij}+\frac{\overline{u_i u_j}}{k}\varepsilon\right]$$

$$\div\left(1+\frac{5\nu}{\varepsilon}f_{\varepsilon}^{*}\frac{\partial k^{1/2}}{\partial x_k}\frac{\partial k^{1/2}}{\partial x_m}\frac{\overline{u_k u_m}}{k}\right) \tag{11}$$

and

$$f_{\varepsilon}=1-\left\{1-\exp\left[-(\tilde{R}_t/80)^2\right]\right\}[1-\exp(-20A^{*1.5})];$$

$$f_{\varepsilon}^{*}=1-\exp[-\tilde{R}_t/(1+2A_2^2)]$$

The quantity f_{ε}^{*}, which is absent from applications of this form at second-moment level, is designed purely to improve the way the fluctuations normal to the wall vanish as the wall is approached.

Finally, it should be noted that Equation 3 does not contain a purely diffusion term; that is to say, a term purely concerned with spatial distribution. However, for numerical stability and the avoidance of unphysical spikiness in A_2, it is expedient to add one. Thus, in place of the terms *containing* diffusive transport

$$\left(-2\frac{A_2}{k}d_k+2\frac{a_{ij}}{k}d_{ij}\right)$$

we adopted the usual generalized gradient transport:

$$d_{A_2}=\frac{\partial}{\partial x_k}\left[\left(\nu\delta_{kl}+c_{A_2}\overline{u_k u_l}\frac{k}{\tilde{\varepsilon}}\right)\frac{\partial A_2}{\partial x_l}\right] \tag{12}$$

where the effective diffusion coefficient for A_2 transport c_{A_2} was taken as 0.22 f_g where the origin and form of f_g is discussed in the following section.

Modeling the k and ε equations

The only process requiring approximation in the k equation is diffusive transport. Some workers have explicitly distinguished transport due to fluctuating pressure and that due to velocity fluctuations (Kawamura and Hada 1992; Nagano and Shimada 1993). While the physical rationale for this strategy is acknowledged, we have found the specific forms suggested sometimes provoked numerical instabilities. Accordingly, our practice has been to retain the usual GGDH model (Daly and Harlow 1970) for the total turbulent diffusion:

$$d_k=\frac{\partial}{\partial x_k}\left[\left(\nu\delta_{kl}+c_k\overline{u_k u_l}\frac{k}{\tilde{\varepsilon}}\right)\frac{\partial k}{\partial x_l}\right] \tag{13}$$

The usually adopted value for c_k is 0.22. However, to accommodate the effect of pressure diffusion the coefficient c_k is taken as 0.22 f_g with

$$f_g=5(\varepsilon/\tilde{\varepsilon})^{1/2}-4(\varepsilon/\tilde{\varepsilon})^{1/4} \tag{14}$$

Here $\tilde{\varepsilon}=\varepsilon-2\nu(\partial k^{1/2}/\partial x_j)^2$ vanishes at the wall (Jones and Launder 1972), but beyond the peak in turbulent kinetic energy, which, in a simply strained wall flow, occurs at about 12 wall units, $\tilde{\varepsilon}$ and ε are essentially equal and the function f_g is then equal to unity.

Following Jones and Launder (1972) and many later studies, the quantity $\tilde{\varepsilon}$ is taken as the subject of the transport equation because of the convenient wall condition $\tilde{\varepsilon}|_w=0$. While closure proposals for the $\tilde{\varepsilon}$ transport pay some attention to the exact form, there is inevitably a great deal of empiricism in arriving at the final form. In the present work, the modelled equation is conveniently written:

$$\frac{D\tilde{\varepsilon}}{Dt}=d_{\tilde{\varepsilon}}+c_{\varepsilon 1}\frac{\tilde{\varepsilon}}{k}P_k-c_{\varepsilon 2}\frac{\tilde{\varepsilon}^2}{k}+P_{\varepsilon 3}+S_{\varepsilon} \tag{15}$$

The second and third terms on the right have the conventional source and sink form present in the earliest proposals. There is, however, an important difference borrowed from the second-moment closure work at UMIST (e.g., Launder and Tselepidakis 1993); namely that, in an anisotropic stress field, $c_{\varepsilon 2}$ should take a lower value than in an isotropic field. Correspondingly, $c_{\varepsilon 1}$ is reduced. Here the form adopted is

$$c_{\varepsilon 1}=1.0+0.15(1-A^{*})$$

$$c_{\varepsilon 2}=1.92/\{1+0.7(R_t/20)^2\sqrt{A}_2\max(0.25,\ A^{*})/[1+(R_t/20)^2]\}$$

The form of the term $P_{\varepsilon 3}$ follows earlier suggestions of Jones and Launder (1972) and Rodi and Mansour (1993) though now generalized to apply to other than a simple shear

$$P_{\varepsilon 3}=c_{\varepsilon 3}\nu\nu_t\frac{\partial^2 U_i}{\partial x_k\,\partial x_j}\frac{\partial^2 U_i}{\partial x_k\,\partial x_j}+c_{\varepsilon 4}\frac{\nu\nu_t}{k}\frac{\partial k}{\partial x_k}\frac{\partial U_i}{\partial x_l}\frac{\partial^2 U_i}{\partial x_k\,\partial x_l} \tag{16}$$

where $c_{\varepsilon 3}$ and $c_{\varepsilon 4}$ are taken as 1.2 and 1.0, respectively.

Under S_{ε} are included two terms that are designed to remove significant anomalies. The usual $\tilde{\varepsilon}$ (or ε) equation returns excessive length scales in separated flow unless some device is employed to reduce them. A common practice is to add the so-called "Yap-correction" to the source term, which has the effect of raising ε if the length scale is locally larger than it would be in a local equilibrium shear flow. This term, however, contains the normal distance to the wall and is known to perform poorly on surfaces of complex shape. Accordingly, a replacement has been devised. The basic candidate form explored was

$$c_{\varepsilon 5}\left(\frac{\partial U_l}{\partial x_m}\frac{\partial \phi_1}{\partial x_l}\frac{\partial \phi_2}{\partial x_m}\right)$$

where the ϕs are dependent such variables as k or ℓ raised to some power. The term is negligible in a thin shear flow, because the mean velocity is then very small in directions with appreciable k or ℓ gradients. A second term is added to S_{ε} to balance the viscous diffusion in the vicinity of the wall (Kawamura and Kawashima 1994). The form adopted

$$\frac{-(\varepsilon-\tilde{\varepsilon})}{k}\tilde{\varepsilon}\exp(-\tilde{R}_t^2/4)$$

ensures a balance to first order with $\nu \partial^2 \tilde{\varepsilon}/\partial x_j^2$. Thus

$$S_\varepsilon = \frac{-(\varepsilon - \tilde{\varepsilon})}{k} \tilde{\varepsilon} \exp(-\tilde{R}_t^2/4) + c_{\varepsilon 5} \left(\frac{\partial U_l}{\partial x_m} \frac{\partial \ell}{\partial x_l} \frac{\partial \ell}{\partial x_m} \right) \times \left(\frac{\partial U_p}{\partial x_q} \frac{\partial \ell}{\partial x_p} \frac{\partial \ell}{\partial x_q} \right) \frac{k(\varepsilon - \tilde{\varepsilon})}{\varepsilon} \quad (17)$$

The presently optimized value of the coefficient $c_{\varepsilon 5}$ is 35.0.

Applications of the model

Fully turbulent flows

Craft et al. (1995) discuss the application of the present model to a number of fully turbulent flows. Here, briefly, to review the model performance in that limit, Figures 2–4 show the outcome of applying the model to plane channel flow and to two other wall flows involving streamline curvature. From Figure 2 it is seen that, in plane channel flow, at Re = 13750, the normal stress distributions are, indeed, faithfully captured. In particular, the normal stress level perpendicular to the wall is satisfactorily reproduced, a feature which is crucial to predicting heat transfer rates correctly. The shear stress, which alone affects the mean velocity distribution, is also mimicked accurately and, in consequence, the computed mean velocity profile accords closely with the DNS simulations. It is noted, too, that the predicted energy dissipation rate exhibits the correct variation across the near-wall sublayer with a maximum value at the wall and a saddle point at $y^+ \approx 10$. This is a consequence of the novelties introduced to the $\tilde{\varepsilon}$ transport equation. Suga (1996) shows other results for pipe and channel flow at different Reynolds numbers computed with comparable levels of success.

Figure 3 considers the case of axisymmetric flow through a pipe that rotates about its own axis. The laser-Doppler anemometer (LDA) measured swirl velocity varies in a roughly parabolic

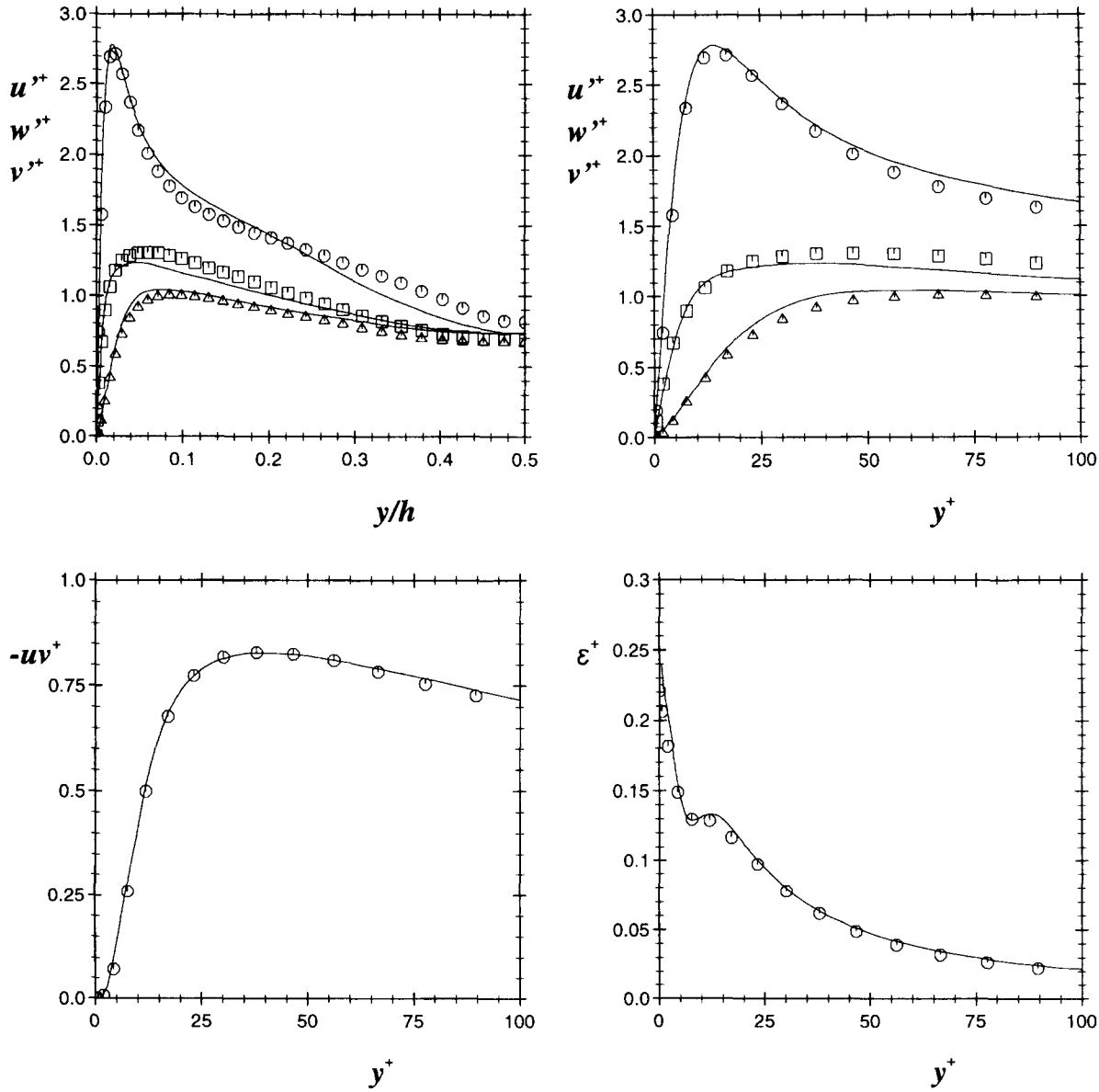

Figure 2 Prediction of fully developed flow in a plane channel at Re = 13, 750. Symbols: NDS results, Kim (1989), ——: computation, present N-LEVM; - - - -: computation using Launder–Sharma (1974) EVM

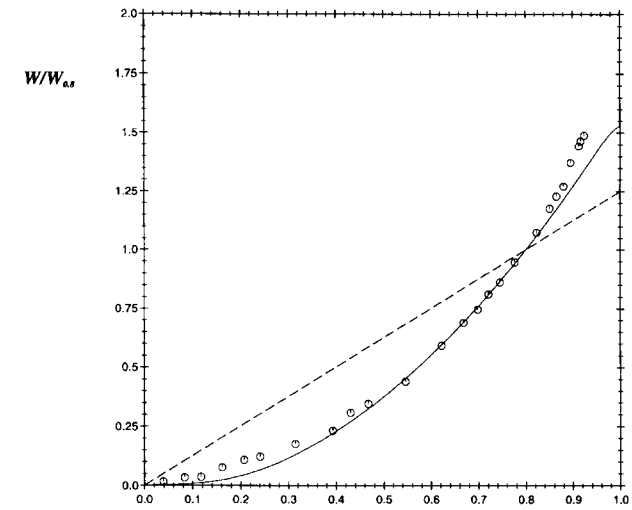

Figure 3 Variation of swirl velocity across pipe rotating about its own axis; symbols: experiments, Cheah et al. (1993); ——: computation, present N-LEVM; - - - -: variation, using any linear EVM.

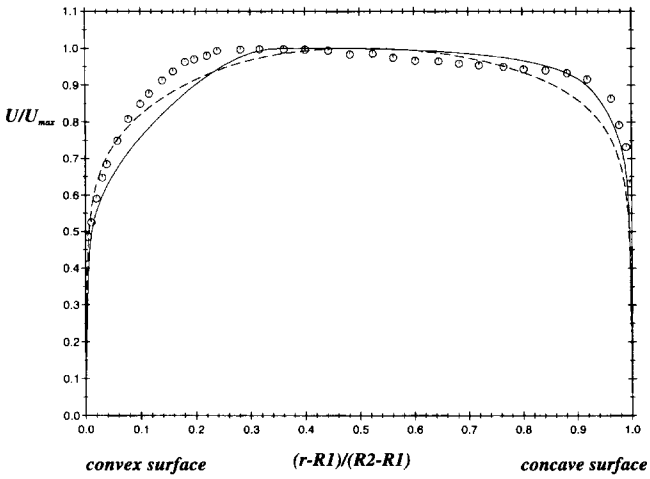

Figure 4 Fully developed flow in a curved channel; symbols: experiment, Ellis and Joubert (1974); ——: present N-LEVM; - - - -: Launder-Sharma (1974) EVM

manner from the axis to the wall; whereas, any linear eddy-viscosity model gives a linear variation (solid-body rotation) once the flow is fully developed. It is seen, however, that the N-LEVM mimics the measured variation very closely.

Finally, the mean velocity profile for the fully developed flow in a curved channel is shown in Figure 4. The strongly asymmetric character of the flow measured by Ellis and Joubert (1974) is captured much better with the nonlinear EVM than with the Launder–Sharma (1974) linear EVM. However, it can be noted that, for the flow near the convex surface, the boundary layer is too thick, a consequence of the wall shear stress being too high. Comparisons with the earlier Eskinazi and Yeh (1956) data showed a much smaller anomaly, however, and for that reason, no clear signals were provided on whether some retuning (of c_7 and, possibly, c_5) would have been appropriate. This is a topic to which we return in considering the flow around a turbine blade.

Diffusion-controlled transition on a flat plate

Two widely examined test cases measured by a team at Rolls Royce plc are considered where transition is driven by the external free-stream turbulence rather than by the development of Tollmien–Schlichting waves. The cases, designated T3A and T3B, correspond with nominal free-stream levels of 3% and 6%, respectively.

These two-dimensional (2-D) flows have been computed using an elliptic flow solver, STREAM, Lien and Leschziner (1994), employing a collocated grid. While the scheme is a general, nonorthogonal solver, for these flows a strictly orthogonal mesh

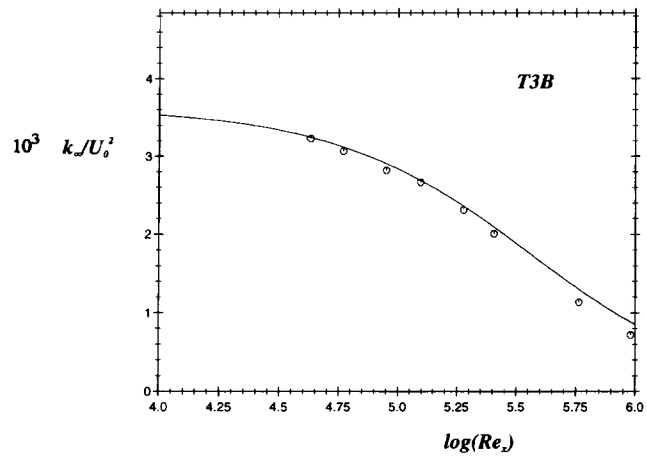

Figure 6 Decay of free-stream kinetic energy for T3B test case; symbols: experiments ——: N-LEVM computations

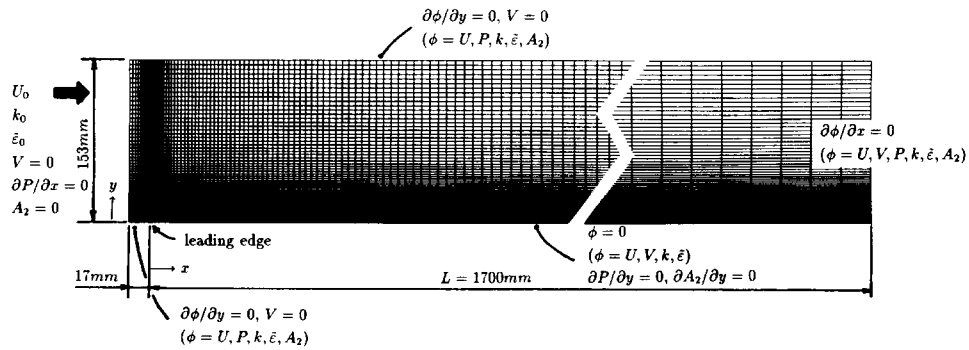

Figure 5 Grid and boundary conditions used for transition prediction on a flat plate

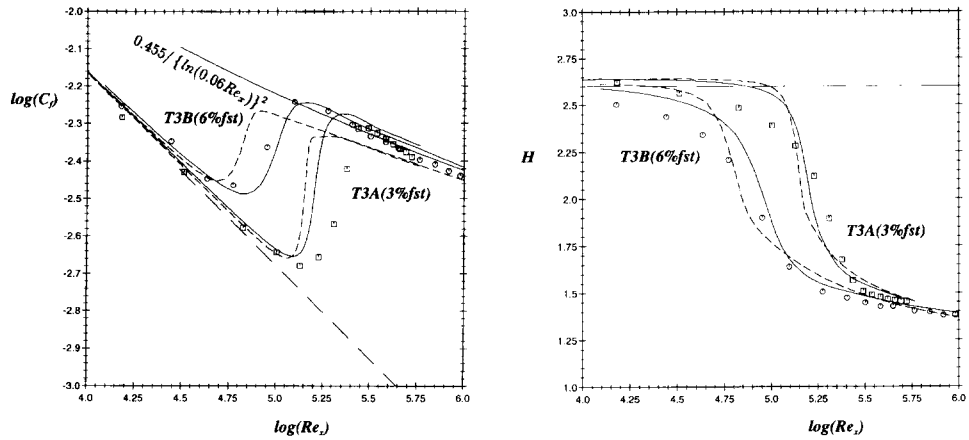

Figure 7 Predictions of skin friction and shape factor for T3A and T3B test cases; symbols: experiments, ——: present N-LEVM; - - - -: Launder–Sharma (1974) EVM; a) skin friction coefficient; b) shape factor

is adopted. A range of grid densities was explored, and, for the final computations, a mesh of 155 (streamwise) × 120 (normal to wall) was adopted for T3A and 80 × 70 for T3B. In both cases, the near-wall node was located at y^+ less than 0.3. A finer mesh was needed at the lower free-stream turbulence, where a lower level of numerical error could be tolerated because of the weaker "disturbance" signal from the background turbulence. Computations began ahead of the leading edge. This was vital, because it enabled uniform profiles of k and ε to be assigned. (If one starts computations on the plate itself, the predicted transition point is strongly dependent on the assumptions made about the way k and ε vary across the boundary layer.) As a consequence, a considerably reduced streamwise internodal spacing was needed in the vicinity of the leading edge of the plate, Figure 5. The actual upstream values of k and ε were chosen to produce broadly the correct initial decay of k with distance *in the free stream*, Figure 6. The initial condition assigned to A_2 was zero, since, in the absence of mean strain, the values of all the a_{ij} given by the N-LEVM formula, Equation 1, would be zero. This isotropic stress field does not quite accord with the experimental data but, at this level of modeling, such transport effects cannot be accounted for.

The variation of the computed transition indicators, the skin friction coefficient c_f, and the shape factor H is shown in Figure 7 compared with the measurements and the linear k–ε model of Launder and Sharma (1974). This last scheme had been found by Savill (1993) to be the most successful of the linear EVMs in predicting this type of flow, although this conclusion had been reached from calculations adopting parabolic solvers. Evidently, both schemes *do* predict a transition broadly as indicated by the

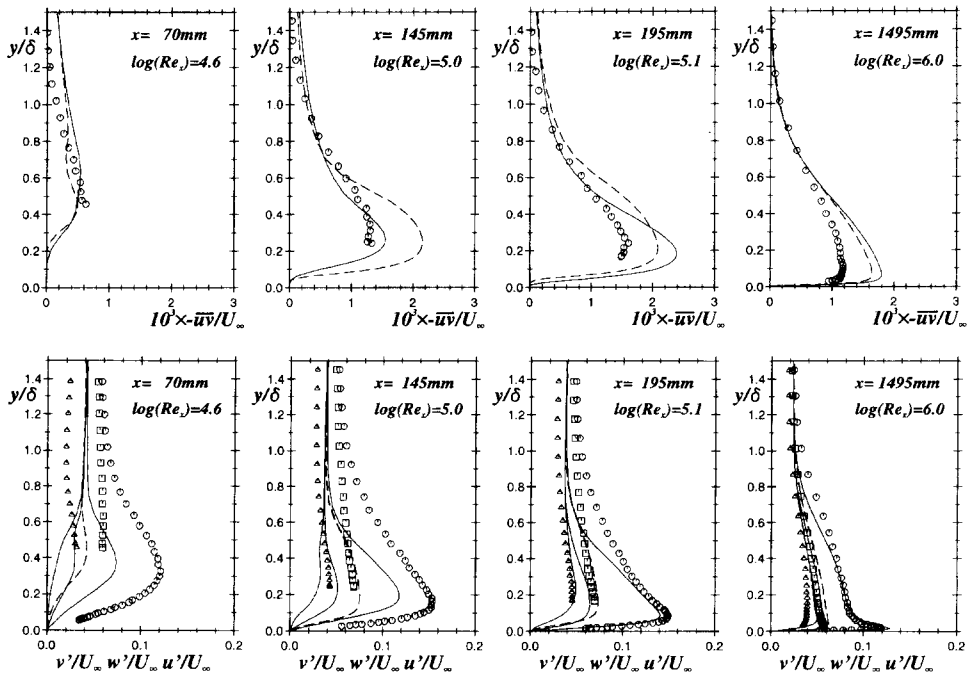

Figure 8 Test case T3B: development of turbulent stresses; key: as Figure 7; a) turbulent shear stress; b) turbulence intensities

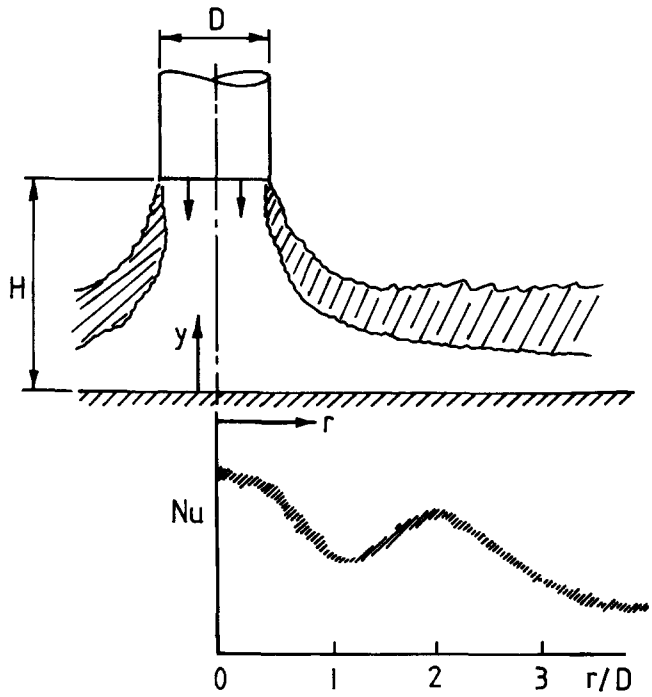

Figure 9 Schematic of features of turbulent impinging jet

data. However, the variation of skin friction computed with the N-LEVM predicts an overshoot following transition in line with experiment. In contrast, the linear EVM, after the transitional region, gives values of c_f below the fully turbulent line. Minor improvements from adopting the nonlinear scheme are also evident in the shape factor, particularly at the higher turbulence level. For the higher free-stream turbulence, the distribution of the shear stress and the rms turbulence intensities are shown in Figure 8 at four representative positions in the transition process. Generally, the build-up of the turbulent shear stress is well captured except that, toward the end of transition, the measured turbulent shear stress is some 35% below the prediction. It seems probable that this is an experimental error, since there is close accord with the independently measured wall shear stress. The turbulence intensity distributions broadly capture the build-up of the individual fluctuations, although, in the early stages of transition, the predicted rise of turbulence near the wall is not as rapid as the experiments indicate. As with the channel flow considered earlier, any linear EVM can achieve no discrimination in the turbulent fluctuations in different directions.

Turbulent impinging jet

While purists might argue whether this case is strictly one of diffusion-controlled transition, it is unquestionably closely related to it; moreover, it is manifestly relevant to by-pass transition on a turbine blade to be considered later. As indicated in Figure 9, fully developed turbulent flow from a pipe impinges normally onto a smooth wall, producing an axisymmetric radial wall jet. When the jet discharge is close to the wall, ($H/D = 2.0$), the mixing layer formed at the edge of jet does not impinge directly onto the plate, but the larger scales and enhanced turbulence levels in the mixing layer lead to a strong rise in

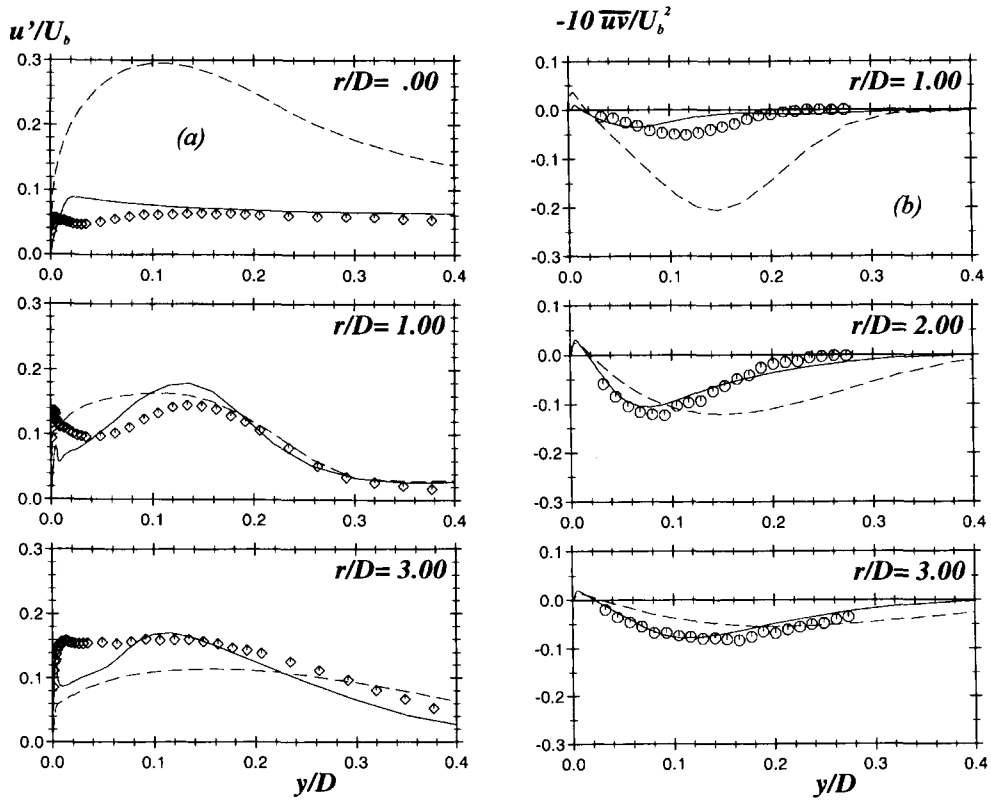

Figure 10 Development of turbulent dynamic field of impinging jet for $H/D = 2.0$; key: as Figure 7; experiments of Cooper et al. (1993); a) rms velocity fluctuations in direction of mean velocity; b) turbulent shear stress

Nusselt number at a radius of about 2D from the stagnation point. As H/D is increased, the link to diffusion-controlled transition becomes more tenuous: for example, at $H/D = 6$, the secondary peak in Nusselt number disappears. Nevertheless, for completeness, that limit is also examined.

First, Figure 10 shows the measured turbulence intensity in the direction of the mean velocity vector, which is approximately what the single normal hot-wire will have recorded (Cooper et al. 1993). At $r/D = 0$ this amounts to the variation of turbulent velocity along the stagnation streamline. As is well known, any linear EVM leads to excessive normal stress levels approaching a stagnation point due to the inappropriate stress-strain connection for an irrotational stagnation flow implicit in the basic constitutive equation. The nonlinear EVM, however, does very much better. Once the flow has been deflected to flow radially outward (so the stresses are principally determined by the primary shear, $\partial U/\partial y$), there is less difference between the linear and nonlinear results. However, the N-LEVM returns far more realistic levels of shear stress, and, as a consequence, the growth of the mean velocity profile (in the form of a radial wall jet) is significantly less than with the linear EVM, Figure 11. It is noted that between the stagnation point and $r/D = 2$ the near-wall fluctuating velocity levels rise from about $0.05U_b$ to $0.2U_b$ representing at least a tenfold increase in k. It is this rise that creates the increase in Nusselt number referred to above and shown, now, in quantitative terms, at two Reynolds numbers in Figure 12. It is noted that the nonlinear EVM achieves more realistic levels of Nu at the stagnation point and, as a result, a secondary peak in Nusselt number is, indeed, predicted. One less satisfactory feature of the prediction is that the dependence of this second peak in Nusselt number on Reynolds number is not correctly captured (the experiments show very nearly a variation as $\mathrm{Re}^{0.7}$; whereas, the N-LEVM indicates the second peak varies as $\mathrm{Re}^{0.9}$). This is something that, for the future, needs re-examining. It is worth remarking that our earlier two-equation N-LEVM, which employed the "Yap correction" in the ε equation, showed a smaller error of this type, Craft et al. (1993, 1996). Finally, for interest, Figure 13 compares the profiles of the flatness factor A obtained from processing the stress field with that from solving the A_2 transport equation (A^*). Both formulations correctly lead to a zero value at the wall but, inevitably, the directly processed value from Equation (1) leads to (very nearly) the isotropic value of 1.0 in the wall jet at the point of velocity maximum. The value A^*, computed from the A_2 equation, does not exhibit this anomaly: indeed, precisely because the A_2 equation contains *transport* agencies, A^* displays more the type of behavior that must actually occur in this flow.

As a footnote to these predictions, Figure 14 considers the case where the jet discharges six diameters above the plate. In that case, the turbulence levels at the stagnation point are higher

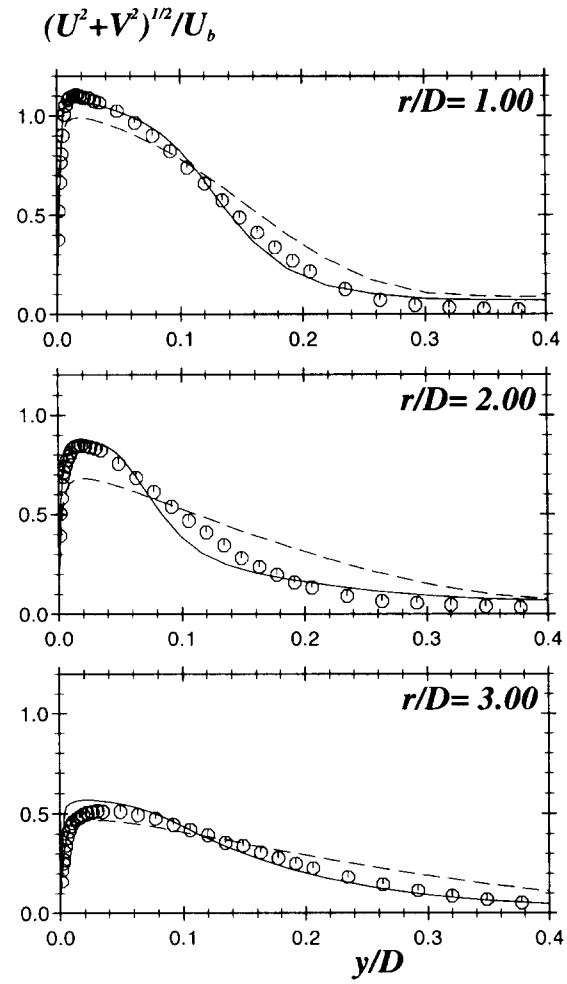

Figure 11 Mean radial velocity field in turbulent impinging jet; key as Figure 10

because the axisymmetric mixing layer springing from the jet lip has merged to the jet axis. There is, in consequence, a rapid rise (transition) in wall turbulence, the peak near-wall level being reached at $r/D = 0.5$. There is, thus, no secondary peak in Nusselt number evident. Overall, the N-LEVM predicts the observed mean-field behavior very successfully, although the rather uniform level of the streamwise turbulence intensity out to values of r/D of 2.0 is not particularly well captured.

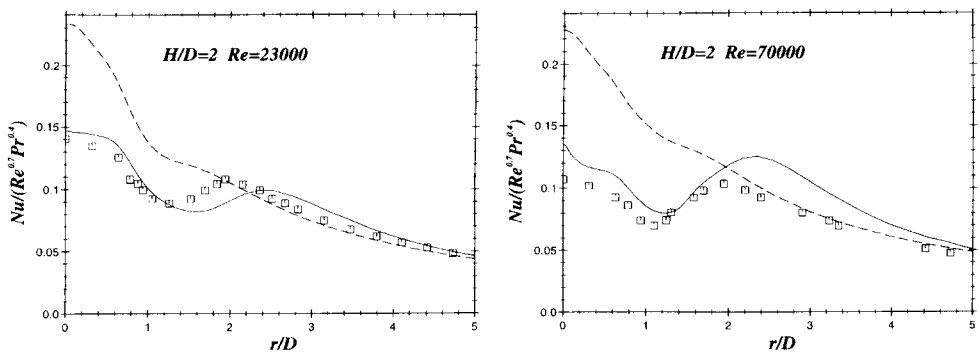

Figure 12 Radial variation of Nusselt number in turbulent impinging jet, $H/D = 2.0$

Flow around a turbine blade

The flow around a turbine blade can be regarded as a combination of a boundary layer and a stagnation flow so the simpler test cases considered above may be seen as an appropriate pre-enquiry. The test cases chosen were a sequence at the lowest exit Mach number 0.78 from the experiments of Nicholson et al. (1982) of flow through a linear, "low-stagger" cascade of rotor blades. These workers had confirmed that the flow was 2-D over the central 60% of the flow. The nominal free-stream turbulence intensity was 4%, and experiments were made at the design flow rate (which gave a chord Reynolds number of 1.113×10^6 based on exit velocity) and at flow rates above and below design ($Re_c = 0.557 \times 10^6$ and 1.67×10^6). Further details of the experiments are provided in Nicholson et al.

The solver adopted was originally coded for incompressible flows and while, as noted, the lowest Mach number was selected, nevertheless some adaptations were needed for this test case. Firstly, density variation effects needed inclusion in the pressure-correction equation to account for the fact that now a modification to the pressure results in updates to both velocity components and the density. Moreover, in solving the thermal energy equation, viscous dissipation terms were added. The local density itself was computed from the ideal-gas equation of state, while the dependence of the dynamic viscosity and thermal conductivity on temperature was included. Finally, in the turbulence modeling equations, the strain tensor S_{ij} has been replaced by the traceless form S'_{ij} where

$$S'_{ij} \equiv S_{ij} - \frac{1}{3}\delta_{ij}S_{kk}$$

This was essential, otherwise the contraction a_{kk} would not be zero.

Figure 15 shows the mesh adopted, a 320 (circumferential) × 100 nonorthogonal 0-type grid generated by the smoothed "trans-finite interpolation" method described in Thompson et al. (1985). This mesh type led to acceptable near-wall cell configurations including the stagnation and trailing-edge regions. A defect with this gridding arrangement arises in the wake region where there is inevitably appreciable flow-to-grid skewness in the wake.

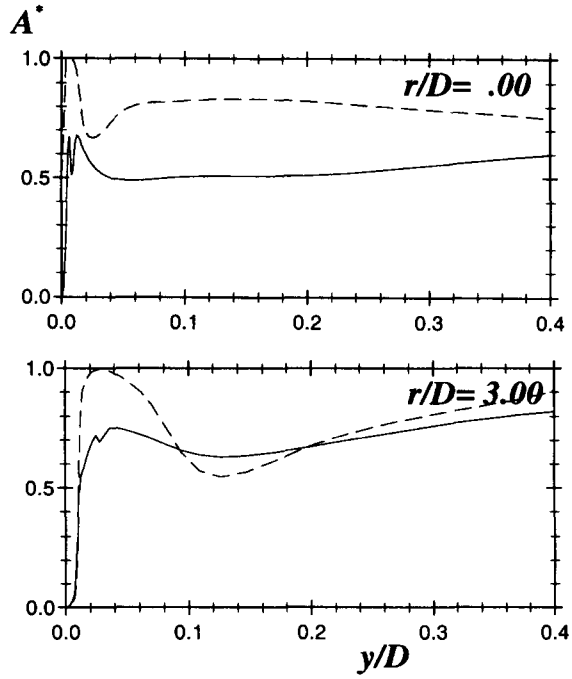

Figure 13 Variation of flatness parameter in impinging jet; ---- A from processing the resultant stress field (given by Equation 1); —— A^* using transport equation for A_2

This made it difficult to achieve fully grid-independent results, even though a higher-order convection scheme was adopted. Fortunately, in the present application, attention was focused on the behavior on the blades, and, since there was no downstream flow recirculation, any imperfections in resolving the wake did not feed back upstream.

Computations of the equivalent isentropic surface Mach number M_s for the design Reynolds number are shown in Figure 16. On the suction surface, the flow accelerates up to 70% chord before decelerating modestly, while, on the pressure surface, a

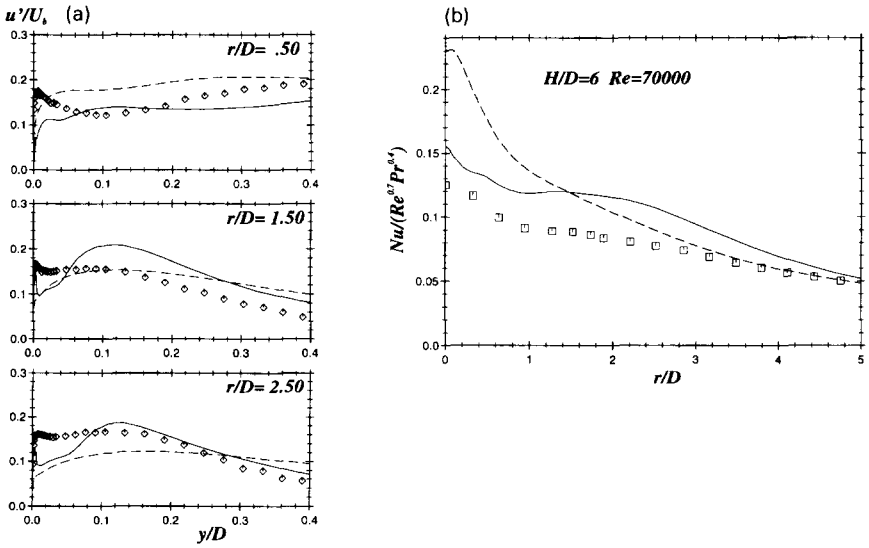

Figure 14 Turbulent impinging jet, $H/D = 6.0$; key as Figure 7; a) streamwise turbulence intensity; b) Nusselt number

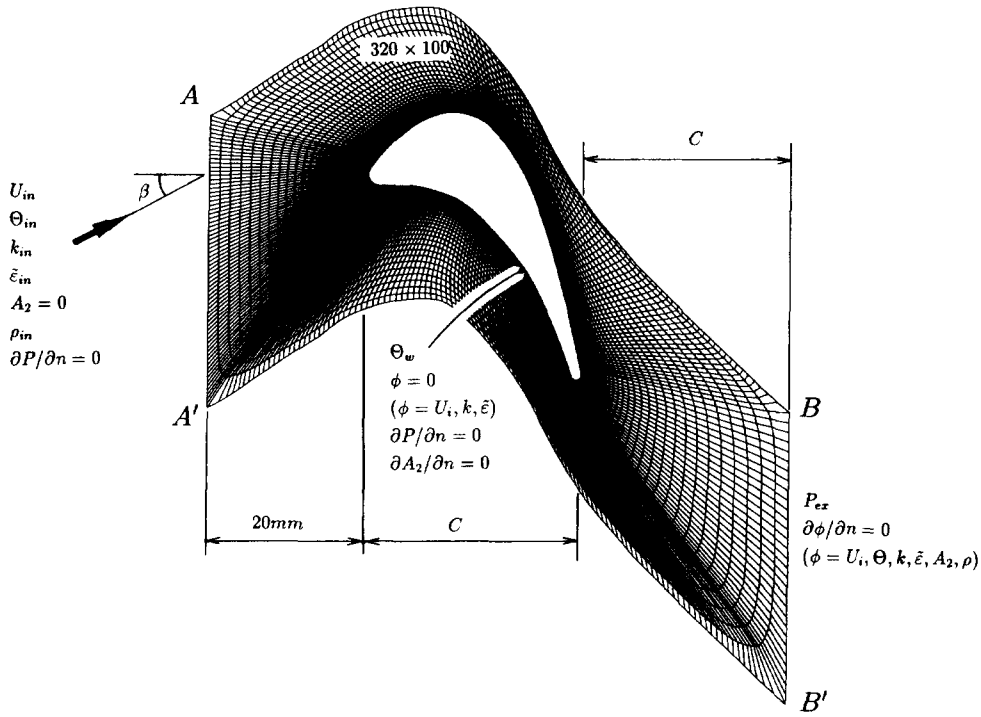

Figure 15 Mesh adopted for flow around a turbine blade

mild acceleration over most of the blade becomes markedly more severe toward the trailing edge. The N-LEVM evidently captures the variation of M_s more successfully than the linear model, where the stagnation region followed by the strong acceleration leads to excessive turbulence energy levels (Figure 17). Note that energy generation arises from the severe normal straining of the flow both in the stagnation zone and in the accelerating region. The energy generation by such normal straining is:

$$-\left(\overline{u^2}\frac{\partial U}{\partial x} + \overline{v^2}\frac{\partial V}{\partial y}\right)$$

and with a linear EVM this term gets represented as:

$$4\nu_t\left(\frac{\partial U}{\partial x}\right)^2$$

(neglecting the effect of density gradients). This is what leads to the very high levels of k over the downstream portion of the blade, a feature that is absent when the N-LEVM is adopted.

While no direct measurement of turbulence energy are available, we can infer that the high predicted turbulence levels are spurious from the excessive levels of heat transfer generated with the linear EVM shown in Figure 18. A behavior much closer to that measured is obtained with the N-LEVM. Nevertheless, while agreement with experiment is excellent on the concave pressure surface, the computed boundary layer on the suction surface undergoes transition too soon, at all Reynolds numbers.

At first the possibility that the input initial turbulence level was too high was considered a possible source of error, or, that the initial level of ε was assigned a too small value. Accordingly, a further calculation was made with ε_o increased by a factor of 5 and k_o decreased by 25% (this, we felt, was the maximum likely errors in the initial values present in the experiments). In fact, this change had no significant effect on where transition occurred. It was, therefore, concluded that the model, as presented, tends to give a too rapid transition on a convex surface. Looking back to the fully turbulent flow through a curved channel (Figure 3), it is evident that there, too, on the convex surface, there was an insufficient damping of turbulent transport. Evidently, therefore, a modest recalibration of the coefficients in the stress-strain equation seems to be needed to see whether this anomaly on convex surfaces can be eliminated or at least reduced. Notwith-

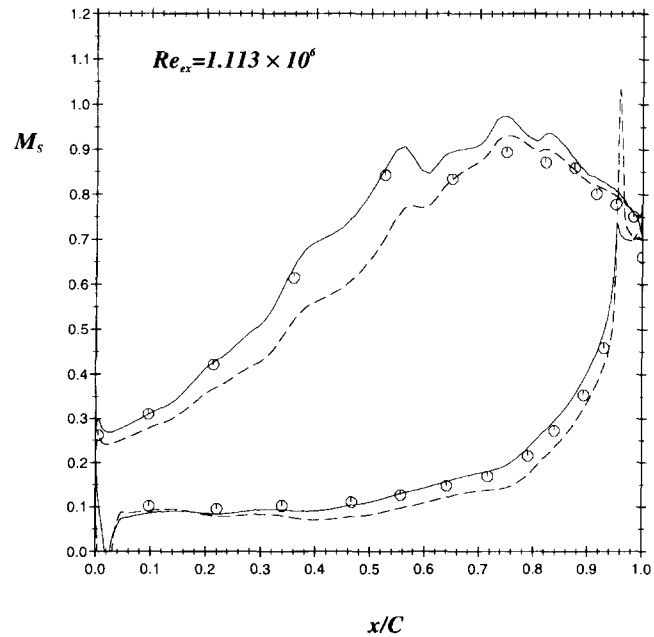

Figure 16 Variation of isentropic Mach number around blade; symbols: experiments, Nicholson et al. (1982); ——: present N-LEVM predictions; - - - -: predictions using L-S EVM

Figure 17 Levels of turbulent kinetic energy through cascade: a) present N-LEVM predictions; b) L-S EVM predictions

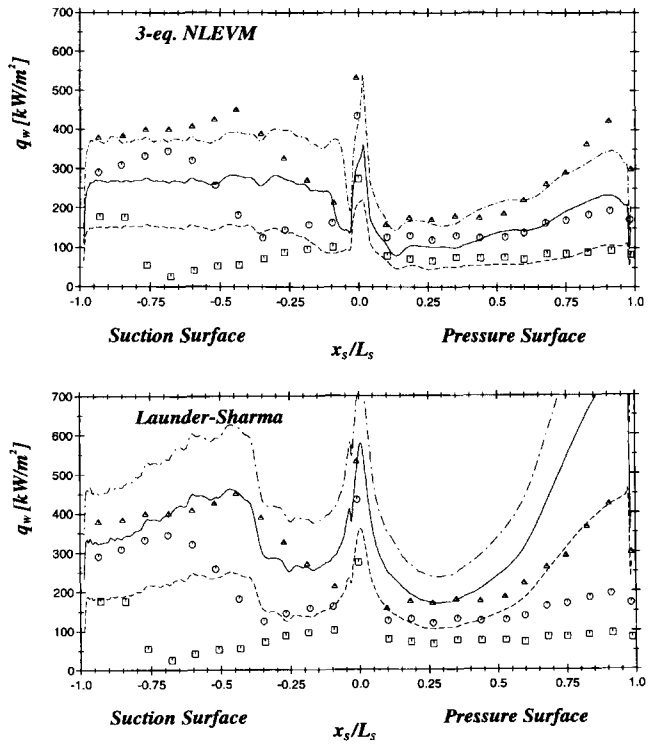

Figure 18 Predicted variation of Nusselt number around blade at three Reynolds numbers; symbols: experiments, Nicholson et al. (1982); lines: computations a) present N-LEVM model; b) L-S EVM predictions

standing this weakness, however, the cubic nonlinear EVM evidently gives a much more satisfactory account of the variation of heat transfer coefficient around the blade surface that the linear model.

Concluding remarks

A new nonlinear eddy-viscosity model has been presented that is designed to handle nonequilibrium low-Reynolds number phenomena, especially that of by-pass transition beneath a turbulent external stream. The novel features of the model in comparison with existing N-LEVMs are

(1) the inclusion of cubic contributions from the mean strain and vorticity tensors that enable the stress field to be made sensitive to streamline curvature; and
(2) the use of a transport equation for the stress-anisotropy invariant, A_2, which enables the normal stresses in the near-wall sublayer to be far better resolved.

Despite the far more elaborate constitutive equation and the solution of the extra equation for A_2, our experience is that the computing time required is normally only about 20% more than for a low-Re linear k-ε model.

Moreover, applications have shown the model to be far more reliable than the *linear* EVM, particularly in impinging flows and in other situations where normal straining is a major contributor to stress generation. A defect in the model has emerged on convex surfaces, however, where insufficient damping of the stress field results. Thus, for the future, a careful recalibration of the empirical coefficients seems desirable. If by-pass transition on turbine blades is the principle flow of interest, the types of strain field arising in such flows should especially be taken into account in any recalibration.

Acknowledgments

The STREAM computer program was kindly made available by F-S Lien who also offered helpful advice on its adaptation at different times in the research. KS acknowledges with thanks the support of Toyota Research Laboratories throughout his Ph.D. studies. The project has been carried out as a part of a research program for Rolls Royce plc. M. Curtis has compiled the manuscript. Authors' names are sequenced alphabetically.

References

Cheah, S. C., Cheng, L., Cooper, D. and Launder, B. E. 1993. On the structure of turbulent flow in spirally fluted tubes. *Proc. 5th IAHR Conference on Refined Flow Modelling and Measurements*, Paris, 293–300

Cooper, D., Jackson, D. C., Launder, B. E. and Liao, G. X. 1993. Impinging jet studies for turbulence model assessment. Part 1: Flow-field experiments. *Int. J. Heat Mass Transfer*, **36**, 2675–2684

Craft, T. J. and Launder, B. E. 1992. New wall-reflection model applied to the turbulent impinging jet. *AIAA J.*, **30**, 2970

Craft, T. J. and Launder, B. E. 1995. Improvements in near-wall Reynolds stress modelling for complex flow geometries. *Proc. 10th Symposium on Turbulent Shear Flows*, The Pennsylvania State University, University Park, PA

Craft, T. J., Launder, B. E. and Suga, K. 1993. Extending the applicability of eddy-viscosity models through the use of deformation invariants and non-linear elements. *Proc. 5th Int. Symposium Refined Flow Modeling and Turbulence Measurements*, Presses Ponts et Chausees, Paris

Craft, T. J., Launder, B. E. and Suga, K. 1995. A non-linear eddy viscosity model including sensitivity to stress anisotropy. *Proc 10th Symposium on Turbulent Shear Flows* pp. 23/19–23/25, Pennsylvania State University

Craft, T. J., Launder, B. E. and Suga, K. 1996. Development and application of a cubic eddy-viscosity model of turbulence. *Int. J. Heat Fluid Flow*, **17**, 108–115

Daly, B. J. and Harlow, F. H. 1970. Transport equations in turbulence. *Phys. Fluids*, **13**, 2634–2649

Ellis, L. B. and Joubert, P. N. 1974. Turbulent shear flow in a curved duct. *J. Fluid Mech.*, **62**, 65

Eskinazi, S. and Yeh, H. 1956. An investigation on fully developed turbulent flows in a curved channel. *J. Aeronaut. Sci.*, **23**, 23–75

Jones and Launder. 1972. The prediction of laminarization with a two-equation model of turbulence. *Int. J. Heat Mass Trans.*, **15**, 301

Kasagi, N., Tomita, Y. and Kuroda, A. 1992. Direct numerical simulation of passive scalar field in a turbulent channel flow. *J. Heat Transfer*, **114**, 598–606

Kawamura, H. and Hada, K. 1992. *Proc. 29th National Heat Transfer Symposium of Japan*, Osaka, 380–382

Kawamura, H. and Kawashima, N. 1994. A proposal of k–ε model with relevance to near-wall turbulence. *Proc. Int. Symposium on Turbulence and Heat Transfer*, Lisbon, Portugal

Kim, J. 1989. Personal communication

Launder, B. E. and Sharma, B. I. 1974. Application of the energy-dissipation model of turbulence to the calculation of flow near a spinning disc. *Lett. Heat Mass Transfer*, **1**, 131–138

Launder, B. E. and Spalding, D. B. 1974. The numerical computation of turbulent flows. *Comp. Methods Appl. Mech. Eng.*, **3**, 269–289

Launder, B. E. and Tselepidakis, D. P. 1993. Contribution to the modelling of near-wall turbulence. In *Turbulent Shear Flows—8*, F. Durst et al. (eds.), Springer, Heidelberg, 81–96

Lien, F. S. and Leschziner, M. A. 1994. A general non-orthogonal finite-volume algorithm for turbulent flow at all speeds incorporating second-moment turbulence-transport closure, Part 1: Numerical implementation; Part 2: Application. *Computer Meth. Appl. Mech. Eng.*, **114**, 123–167

Lumley, J. L. 1978. Computational modelling of turbulent flows. *Adv. Appl. Mech.*, **18**, 123

Nagano, Y. and Shimada, M. 1993. *Proc. 9th Symposium on Turbulent Shear Flows*, (Paper 23-4) Kyoto, Japan

Nicholson, J. H., Forest, A. E., Oldfield, M. L. G. and Schultz, D. L. 1982. Heat transfer optimised turbine rotor blades—An experimental study using transient techniques. ASME paper 82-GT-304

Pope, S. 1975. *J. Fluid Mech.*, **2**, 331–340

Rodi, W. and Mansour, N. 1993. *J. Fluid Mech.*, **250**, 509–529

Savill, A. M. 1993. Some recent progress in the turbulence modelling of by-pass transition. In *Near Wall Turbulent Flows*, R. M. C. So, C. G. Speziale and B. E. Launder (eds.), Elsevier Science, New York, 829–848

Savill, A. M. 1995. ERCOFTAC Bulletin, **24**, 57–61

Scheuerer, G. 1983. Entwicklung eines Verfahrens zur Berechnung zweidimensionaler, Grenzschichten an Gasturbinensschaufeln. Doktor-Ingenieur Thesis, University Karlsruhe, Karlsruhe, Germany

Suga, K. 1996. Development and application of a non-linear eddy-viscosity model sensitized to stress and strain invariants. Ph.D. Thesis, Dept. of Mechanical Engineering, UMIST (Also available as Rept. TDF/95/11, Dept. of Mechanical Engineering, University of Manchester Institute of Science and Technology).

Thompson, J. F., Warsi, Z. U. A. and Mastin, C. W. 1985. *Numerical Grid Generation*. North-Holland, Elsevier